Investigation of Laser Debonding Using a 308 nm Excimer Laser for Advanced Semiconductor Packaging

Insung Choi*[1], Xuan-Bach Le[2], Sung-Hoon Choa[2], Sungwon Mo[3], and Seunghoon Lee[3]

[1]*Center of Innovation Research Strategy & Planning, Korea Institute of Machinery & Materials, 46744, Republic of Korea*
[2]*Intelligent Semiconductor Engineering Department, Seoul National University of Science & Technology, 01811, Republic of Korea*
[3]*R&D Center, ZEUS Co., Ltd, 18363, Republic of Korea*
** Corresponding author's e-mail: ichoi@kimm.re.kr*

The semiconductor packaging industry requires ultrathin device wafers to achieve high-density vertical integration and high performance. However, ultrathin wafers with thicknesses below 30 μm are prone to warpage and fracture. To address this issue, various temporary bonding and debonding technologies have been developed. Among these, laser debonding has attracted significant attention because it enables stress-free separation of temporary bonding wafers. In addition, it provides higher throughput (wafers per hour) than conventional mechanical peel-off methods. In this study, two types of temporary bonding wafers with standard and inverse structures were prepared to investigate the optimal bonding material configuration. Furthermore, two-dimensional transient heat transfer simulations were performed for both structures to understand the thermal response during laser debonding. A 308 nm excimer laser with a homogenized flat-top beam was irradiated through the glass side of both temporary bonding wafers, and comparative studies on various processing parameters were performed. The results indicate that an optimized energy density enables successful debonding without damage to the device wafer, and that the inverse structure is suitable for applications in advanced semiconductor packaging.

DOI:10.2961/jlmn.2026.02.2010
Keywords: advanced packaging, temporary bonding and debonding, laser debonding, excimer laser

1. Introduction

The rapid advancement of high-bandwidth memory (HBM) technology has driven the need for extreme wafer thinning in advanced semiconductor packaging to achieve higher integration density and improved electrical and thermal performance. Modern HBM architectures rely on the vertical stacking of multiple ultrathin silicon dies interconnected by through-silicon vias (TSVs) and dense microbumps, where precise control of wafer thickness and mechanical stability is critical [1–2]. As the thickness of a device substrate (Si wafer) is reduced to the microscale regime, particularly below 30 μm, the wafer becomes increasingly vulnerable to warpage, cracking, and stress-induced damage during handling and postprocessing, rendering conventional mechanical debonding approaches unsuitable. To address these challenges, the Si wafer is temporarily bonded to, and subsequently debonded from, a carrier substrate (glass wafer) to achieve extreme wafer thinning. This process is known as temporary bonding and debonding (TBDB) technology in advanced semiconductor packaging [3–5].

Among the debonding technologies, laser-based substrate separation techniques have been recognized as promising solutions, especially for Si wafer thicknesses below 30 μm, and are commonly referred to as a laser debonding technology. In laser debonding processes, the choice of temporary bonding material (TBM) and laser parameters plays a decisive role in determining debonding reliability and postprocess yield. A typical TBM consists of a laser-absorbing release material and an adhesive material, which together form a temporary bonding wafer (TBW) structure such as glass wafer/release layer/adhesive layer/Si wafer [6–7]. The release material must exhibit suitable optical absorption at the laser wavelength to induce localized thermal decomposition, while maintaining sufficient adhesion to ensure process stability during wafer thinning and device fabrication. Furthermore, laser debonding requires careful consideration of TBM selection with respect to post-debonding residue, cleaning processes, and the absence of thermal damage to microbumps on the device wafer. Notably, significant research efforts in laser debonding have been led by the Shenzhen Institutes of Advanced Technology (SIAT), Chinese Academy of Sciences [8–12]. This research consortium has reported laser debonding mechanisms based on independently designed TBM and a diode-pumped solid-state (DPSS) laser operating at 355 nm with a galvanometer scanner, attributing the debonding behavior to hot-stamping effects and thermoelastic stress waves. However, comparisons of bonding material configurations between the standard structure (glass wafer/release layer/adhesive layer/Si wafer) and inverse structure (glass wafer/adhesive layer/release layer/Si wafer) remain limited, although this distinction directly affects the cleaning process of the device wafer surface immediately after laser debonding.

In this study, laser debonding was investigated using a 308 nm excimer laser with a flat-top beam profile and a TBM consisting of release (T1107) and adhesive (C1301)

material supplied by BrewerBOND. TBWs were prepared with both standard and inverse structures. Laser processing parameters, such as energy density and shot number, were systematically examined using cross-sectional transmission electron microscopy (TEM). Specifically, EDS analyses were carried out on both the residue release on the glass wafer (from the standard structure sample) and the residue release on the Si wafer (from the inverse structure sample). In addition, heat transfer simulations were performed for both standard and inverse TBW structures. The results provide practical experimental parameters for an optimal laser debonding process tailored to TBDB in advanced semiconductor packaging applications.

2. Experimental procedures

Bonding materials T1107 and C1301, supplied by BrewerBOND, were utilized as the release and adhesive materials, respectively. Two types of temporary bonding specimens were prepared: standard-structure and inverse-structure TBW (**Fig. 1**). In the standard-structure TBW, T1107 spin-coated onto a glass wafer was laminated and bonded to C1301 spin-coated onto a Si wafer. By contrast, in the inverse-structure TBW, C1301 spin-coated onto a glass wafer was laminated and bonded to T1107 spin-coated onto a Si wafer. The thicknesses of the spin-coated T1107 and C1301 were 2.2 μm (± 5 %) and 45 μm (± 5 %), respectively. The bonding process was conducted in two sequential steps at 180 and 220 °C, each for 300 s.

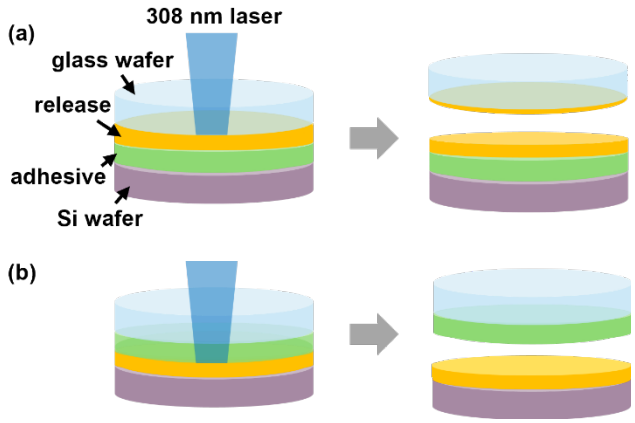

Fig. 1 Schematic of laser debonding process: (a) standard structure and (b) inverse structure.

The laser processing system consisted of a laser source, beam delivery optical system, and X–Y translation stage. **Table 1** summarizes the specifications of the laser system and its primary processing parameters. An excimer laser (LPX Pro 305, Coherent Inc.) emitting radiation at 308 nm was used as the laser source. The maximum repetition rate and pulse energy of the laser were 50 Hz and 600 mJ, respectively. The beam delivery optical system comprised a beam homogenizer and projection lens, enabling a flat-top beam profile with a beam size of 200 mm × 0.4 mm. Based on the beam dimensions, a maximum energy density of 460 mJ/cm² was achieved; however, this study used energy densities in the range of 140 to 300 mJ/cm². The X–Y translation stage was integrated perpendicular to the laser irradiation direction and allowed the loading of substrates up to 8 inches (20.32 cm) in size. For all experiments, the laser repetition rate was fixed at 10 Hz, and the scanning speed along the x-axis was adjusted to achieve a laser beam overlap ratio ranging from 0 to 90 %, corresponding to 1–10 laser shots per position.

Table 1 Specifications of the laser system.

Parameters	Specifications	Used in process
Wavelength (nm)	308	308
Energy density (mJ/cm^2)	max. 460	140~300
Repetition rate (Hz)	max. 50	10
Pulse duration (ns)	25	25
Beam shape	flat-top	flat-top
Beam overlap (%)	0~99	0~90
Beam size (mm)	200 × 0.4	200 × 0.4

Table 2 Simulation parameters.

Simulation variables	Parameters
Laser energy density (mJ/cm^2)	200 ~ 300
Thermal conductivity of T1107 (W/cm·K)	$1.55 \times 10^{-3}(T/T_0)^{0.28}$
Thermal conductivity of glass (W/cm·K)	$7.9 \times 10^{-4}T^{0.43}$
Specific heat of T1107 (J/(g·K))	$2.55 - 1.59 \times \exp[(T_0 - T)/460]$
Specific heat of glass (J/(g·K))	$1.53 - 0.79 \times \exp[(T_0 - T)/638]$
Energy absorption of T1107 (%)	90.2
Density of T1107 (kg/m^3)	1200

Material characterization was performed using various analytical techniques. The thickness and optical constants (refractive index, n, and extinction coefficient. k) of T1107 were measured using an ellipsometer (Elli-SE-UaM8; Ellipso Technology). The optical transmittance of T1107 in the ultraviolet and visible wavelength regions was characterized using a UV–Vis spectrophotometer (Cary 5000, Agilent). After the laser debonding experiments, cross-sectional analyses of the specimens were performed using a focused ion beam (FIB; Helios NanoLab 450, FEI), along with high-resolution and scanning transmission electron microscopy (HRTEM and STEM; JEM-ARM300F, JEOL). Elemental composition analyses were conducted using energy-dispersive spectroscopy (EDS) integrated with STEM.

Transient thermal simulations were conducted to achieve a fundamental understanding of the laser debonding mechanism and validate the experimental optimization results. For a nanosecond pulsed laser operating at an ultraviolet wavelength (308 nm), the photothermal effect is considered the dominant mechanism governing the interaction between the laser beam and release layer [13]. A multilayer finite element heat transfer model was established, consisting of glass (700 μm), release layer (2.2 μm), adhesive layer (50 μm), and Si wafer (725 μm). The heat transfer process during laser irradiation depends strongly on the temperature-dependent thermal properties of the materials. To ensure high accuracy, the specific heat and thermal conductivity of the glass wafer and T1107 were defined as functions of temperature. Here, T_0 denotes the reference temperature corresponding to room temperature (25 °C) used in the temperature-dependent

material properties in **Table 2**. Based on optical property measurements at 308 nm, the 2.2-μm thick T1107 exhibited nearly zero transmission (0.08 %). However, this does not imply that all incident laser energy was absorbed, as surface reflection must also be considered. When surface reflection (~9.7 %) was accounted for, the release layer absorbed approximately 90.2 % of the incident laser energy. To accurately compute the volumetric heat generation and capture the spatial distribution of this absorbed energy along the depth direction, the 2.2-μm thick T1107 was vertically discretized into 10 sublayers. Specifically, the first nine sublayers near the irradiated interface were assigned a fine thickness of 0.2 μm each, while the tenth bottom sublayer had a thickness of 0.4 μm. The simulation systematically investigated laser energy densities ranging from 200 to 300 mJ/cm^2 with a pulse duration of 25 ns. The detailed thermal and physical parameters used in the numerical simulations are summarized in **Table 2** [14–16].

3. Results and discussion

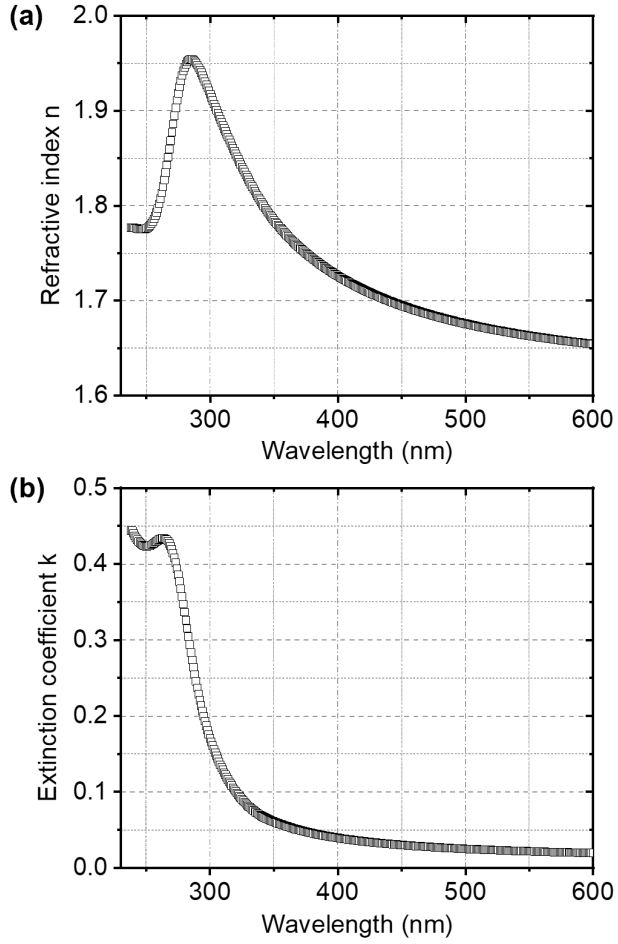

Fig. 2 Optical properties of the release material (T1107). (a) refractive index *n* and (b) extinction coefficient *k*.

Laser debonding is a technique that utilizes temporary bonding between a glass wafer and a Si wafer using a polymer-based bonding material, followed by thinning of the Si wafer and subsequent laser-induced decomposition of the light-absorbing polymer layer. The bonding material consists of release and adhesive materials, and the release material is responsible for absorbing the laser wavelength. Therefore, the characterization of the optical properties of the release material is critical. **Figure 2** shows the refractive index (n) and extinction coefficient (k) of the released material (T1107) as measured via ellipsometry. At a wavelength of 308 nm, the values for n and k were 1.89 and 0.13, respectively. The optical penetration depth (OPD), defined as the distance within a material at which the optical intensity drops to approximately 37 % of its original surface value, can be calculated by equation (1) using k.

$$\delta = \frac{1}{\alpha} = \frac{\lambda}{4\pi k} . \quad (1)$$

where $\delta, \alpha, \lambda,$ and k represent the OPD, absorption coefficient, laser wavelength, and extinction coefficient, respectively. The OPD was approximately 189 nm for a wavelength of 308 nm and the measured k value. The effective penetration depth (EPD), which considers the reflection, transmission, and thickness effects, can be determined using transmittance (T) measurements.

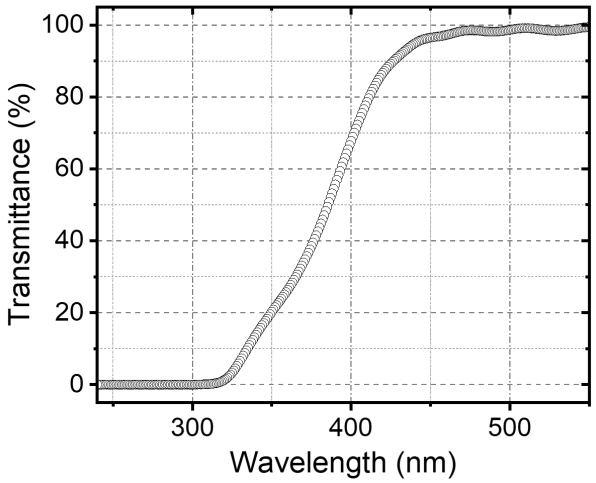

Fig. 3 UV–Vis transmittance spectrum of the release material (T1107).

Figure 3 shows the transmittance data for T1107 obtained using a UV–Vis spectrophotometer. Because material thickness is a critical variable in T data, a thickness of 2.2 μm was used, yielding a T value of 0.1 % at 308 nm. The EPD, derived from the measured T values and the Beer–Lambert law, is given by equations (2), (3), and (4).

$$\delta_{eff} = \frac{1}{\alpha} . \quad (2)$$

$$\alpha = -\frac{1}{L}\ln\left(\frac{T}{(1-R)^2}\right) . \quad (3)$$

$$R = \frac{(n-1)^2+k^2}{(n+1)^2+k^2} . \quad (4)$$

where $\delta_{eff}, \alpha, L, T,$ and R represent the EPD, absorption coefficient, material thickness, measured transmittance, and reflectance, respectively. The EPD of T1107 was approximately 328 nm. A discrepancy was observed between the OPD (based on k) and EPD (based on T). This difference may have stemmed from a slight overestimation of k during the ellipsometric fitting process or minor errors in the UV–Vis measurements owing to the extremely low transmittance. In both cases, the penetration depth ranged from 189 to 328 nm, and thermal decomposition was expected to occur at an even shallower depth near the laser-absorbing surface.

Consequently, employing a microscale-thick release layer in laser debonding prevented thermal damage to the device wafer surface due to laser transmission or heat transfer.

Because laser debonding is a single step in the overall TBDB process, the subsequent cleaning process must be considered when optimizing laser parameters and selecting bonding materials. The cleaning step aims to remove the residual polymers from the device wafer surface. In the standard-structure specimen, residual T1107 and C1301 remained on the Si wafer after debonding. Conversely, in an inverse-structure specimen using a highly transparent adhesive material (e.g., C1301), only T1107 remained on the Si wafer. Although the inverse structure appears to be advantageous for cleaning, few studies have compared the two structures in terms of laser process parameters.

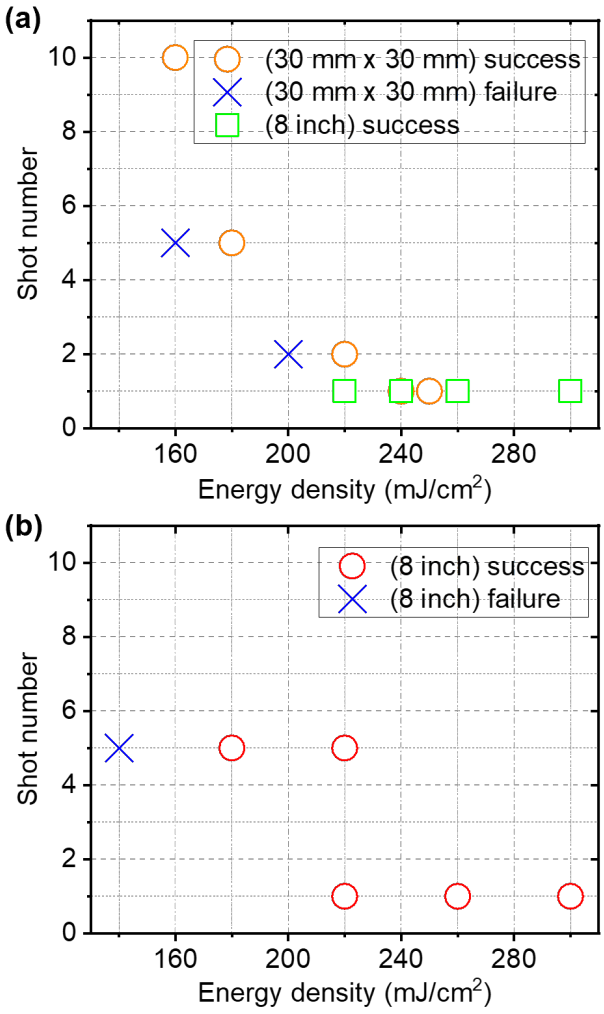

Fig. 4 Laser processing parameters for energy density and shot number: (a) standard structure and (b) inverse structure.

Figure 4 illustrates the relationship between the energy density and shot number (number of laser pulses per unit area) required for the successful debonding of T1107 and C1301. In this study, successful debonding is defined not only as the complete separation of the device wafer from the carrier wafer, but also as the absence of thermal damage to the device wafer surface. Shot numbers of 1, 2, 5, and 10 correspond to beam overlaps of 0, 50, 80, and 90 %, respectively. Generally, a higher energy density reduces the required shot number, whereas a lower energy density requires more shots. Figure 4(a) shows the parameters of the standard-structured TBW specimens. Initial tests on 30 mm × 30 mm samples confirmed that debonding occurred with a single shot at energy densities above 220 mJ/cm². Below this threshold, multishot processing was required; for instance, 160 mJ/cm² enabled debonding but required 10 shots, significantly increasing the processing time. From a productivity standpoint (e.g., wafers per hour or WPH), a single-shot process is preferable. Testing on 8-inch (20.32 cm) wafers at 220–300 mJ/cm² confirmed successful debonding, which was consistent with the 30 mm × 30 mm samples. Figure 4(b) presents the results for the inverse-structure specimen, showing negligible differences in laser parameters compared with those of the standard structure. This observation suggests that C1301 in the inverse structure was transparent to the 308 nm laser wavelength. From a productivity standpoint (e.g., wafers per hour, WPH), a single-shot process is preferable. Therefore, a fluence range of 220–300 mJ/cm² with a single-shot irradiation is recommended for practical manufacturing in both standard and inverse structures.

Figure 5 shows cross-sectional TEM and EDS analyses of residual T1107 on the glass wafer after debonding of a standard-structure TBW at 240 mJ/cm² with 0 % overlap. Figure 5(a) shows an HRTEM image. A Pt protective layer was deposited to prevent surface damage during FIB sampling. The nonuniformity of the Pt coating indicates an uneven surface of the debonded release layer. Although this suggests nonuniformity during the thermal decomposition process, the variance is relatively minor on the nanometer scale. Figure 5(b) shows a magnified view of the square region in Fig. 5(a), where the residual T1107 thickness was measured to be approximately 50 ± 10 nm. STEM imaging and EDS spectra, as shown in Fig. 5(c) and (d), revealed 80.59, 5.14, and 14.27 at% for C, N, and O, respectively. The value for C was only slightly lower than that of the base material (non-irradiated sample), indicating minimal thermal degradation of the residue release layer. Figure 5(e) shows the EDS mapping for Pt, Si, C, and O, confirming the distribution of C between the protective layer and glass substrate. These findings are consistent with those of our previous study using a 355 nm DPSS laser, although the thinner residue layer observed here is likely due to the difference in wavelength [17]. In addition, HRTEM and EDS analyses for samples processed at 160 mJ/cm² with 90 % beam overlap and at 220 mJ/cm² with 50 % beam overlap showed cross-sectional images and atomic percentages comparable to those in Fig. 5, as presented in **Fig. 6**.

Figure 7 presents the cross-sectional TEM/EDS results for the inverse-structure TBW debonded at 220 mJ/cm² with 0 % beam overlap. In contrast to the standard structure, Fig. 7(a) shows a uniform Pt layer, indicating a smooth debonded surface. The residual T1107 thickness was approximately 2.32 μm, as shown in Fig. 7(b). STEM imaging and EDS spectra, as shown in Figs. 7(c) and (d), indicate 89.67, 2.80, and 7.53 at% for C, N, and O, respectively. In a previous study, a sharp decrease in C content (e.g., to 34%) was observed in the heat-affected zone at the laser debonding boundary [17]. Therefore, a C content of approximately 90%, which is comparable to that of the base material, indicates absence of thermal influence. Figure 7(e) shows the EDS mapping for Pt, Si, C, and O, confirming the distribution of

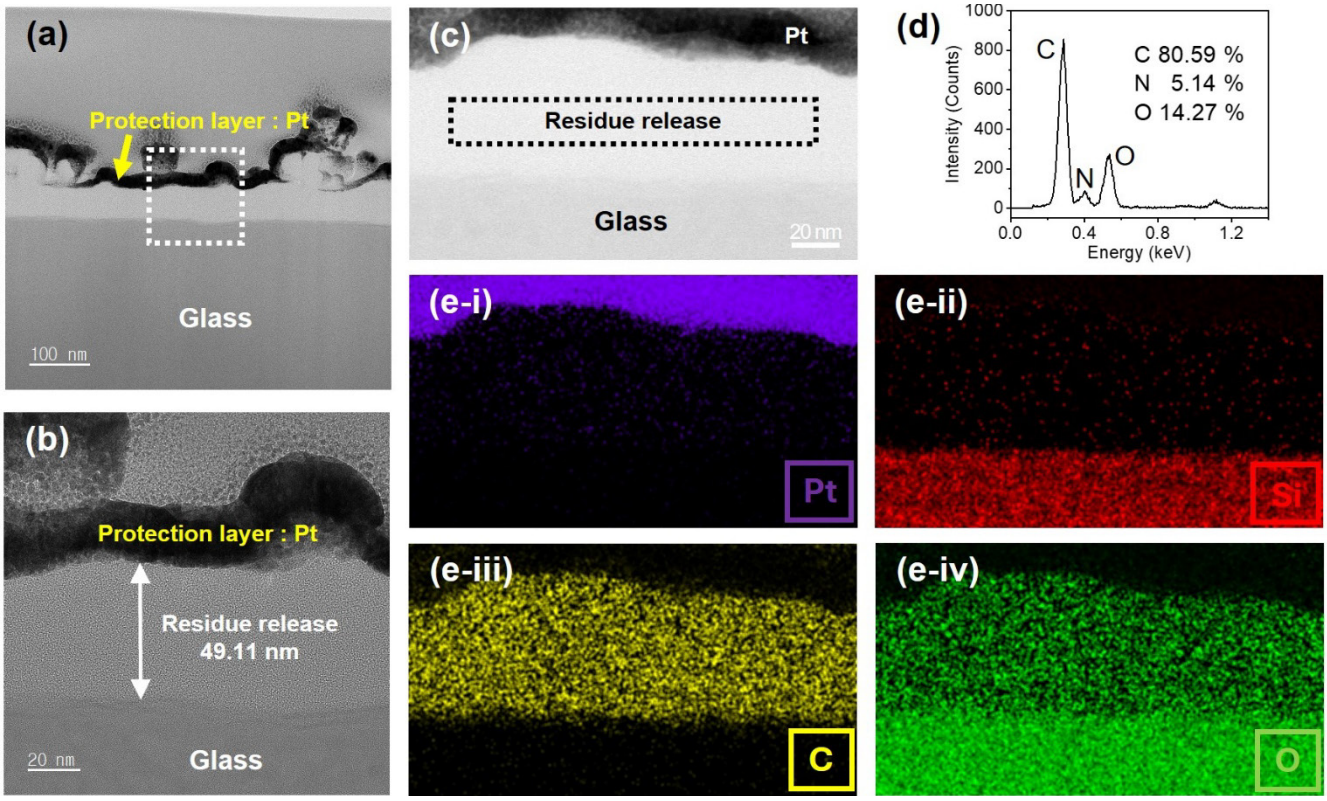

Fig. 5 Analysis of residue release layer in a laser-debonded specimen from the standard-structure TBW. Experimental parameters: 240 mJ/cm^2 and single shot: (a) HRTEM image of the residual release layer on the glass wafer, (b) magnified HRTEM image of the square region in (a), (c) STEM image for EDS analysis, (d) EDS spectrum of residual release layer from the square region in (c), and (e) EDS mapping of Pt, Si, C, and O from (c).

C between the protective layer and the glass substrate. These findings demonstrated complete separation at the interface between the adhesive and release layer. Furthermore, STEM and EDS analyses for samples processed at 260 mJ/cm² with 0 % beam overlap and at 220 mJ/cm² with 80 % beam overlap showed cross-sectional images and atomic percentages comparable to those in Fig. 7, as shown **Fig. 8**.

Feasibility tests for the 8-inch (20.32 cm) inverse-structure TBW were conducted under three different experimental conditions. **Figure 9** shows digital photographs of debonded specimens processed at 260 mJ/cm² with 0 % beam overlap (Fig. 7(a)), 220 mJ/cm² with 0 % beam overlap (Fig. 7(b)), and 220 mJ/cm² with 80% beam overlap (Fig. 7(c)), respectively. The transparency of the adhesive/glass wafer differed slightly depending on the experimental conditions. This variation is attributed to slight differences in carbonization and is not associated with thermal influence on the device wafer surface, as confirmed by the STEM and EDS analyses. Therefore, laser debonding of inverse-structure TBWs appeared suitable for industrial applications.

To obtain a fundamental understanding of the thermal response during laser debonding, a layered two-dimensional transient heat transfer model was established for both standard and inverse temporary bonding wafer structures. The heat conduction equation is expressed by equation (5).

$$\rho C_p \frac{\partial T}{\partial t} = \nabla.(k\nabla T) + Q \ . \qquad (5)$$

where ρ, C_p, k, T, t, and Q denote the density, specific heat, thermal conductivity, temperature, time, and volumetric heat generation, respectively [18–19].

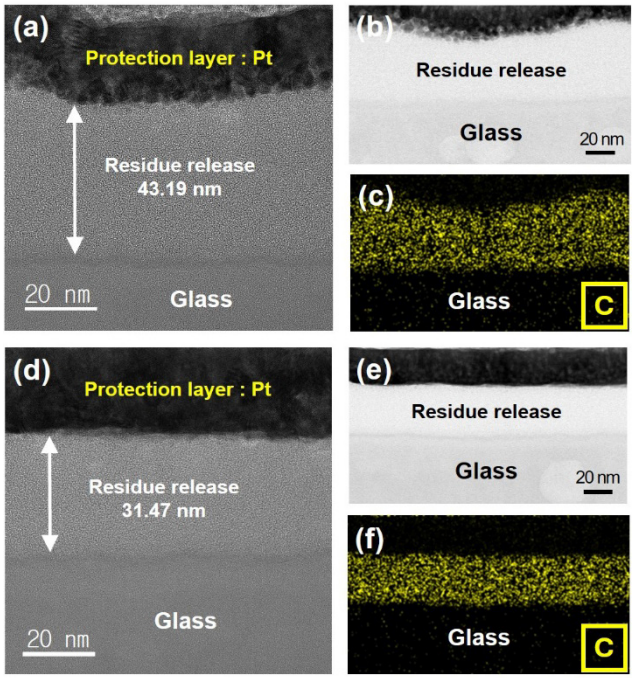

Fig. 6 Analysis of residue release layer in a laser-debonded specimen from the standard-structure TBW. Experimental parameters: 160 mJ/cm^2 and 10 shots: (a) HRTEM image of the residual release layer on the glass wafer, (b) STEM image for EDS analysis, and (c) EDS mapping of C from (b). Experimental parameters: 220 mJ/cm^2 and 2 shots: (d) HRTEM image of the residual release layer on glass, (e) STEM image for EDS analysis, and (f) EDS mapping of C from (e).

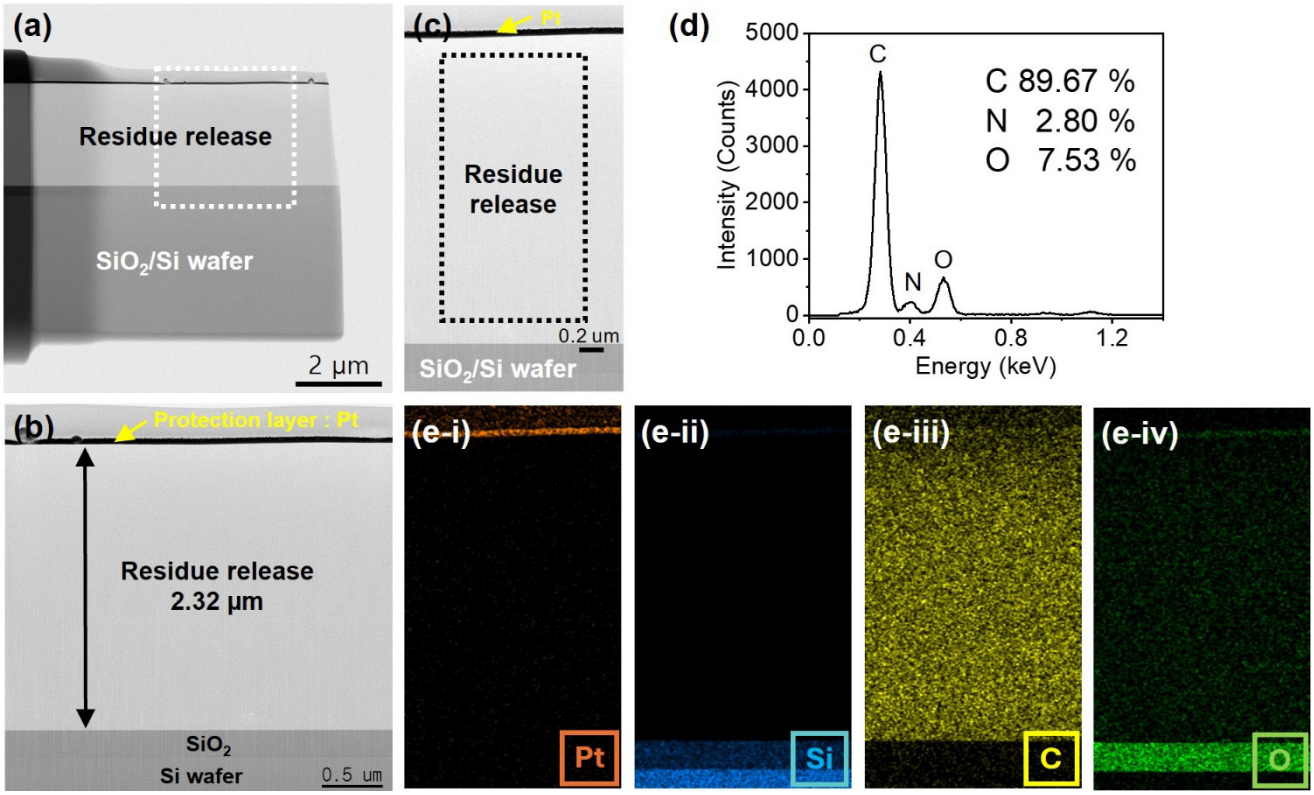

Fig. 7 Analysis of the residual release layer in a laser-debonded specimen from the inverse-structure TBW. Experimental parameters: 220 mJ/cm^2 and single shot: (a) STEM image of the residual release layer on the SiO_2/Si wafer, (b) magnified STEM image of the square region in (a), (c) STEM image for EDS analysis, (d) EDS spectrum of the residual release layer from the square region in (c), and (e) EDS mapping of Pt, Si, C, and O from (c).

Because the 308 nm excimer laser pulse used in this study had a flat-top spatial profile and a pulse duration of 25 ns, the laser energy absorbed in the release layer was modeled as a transient volumetric heat source based on the Beer–Lambert law. The heat generation in the T1107 layer is expressed by equation (6).

$$Q(z,t) = (1-R)\alpha I(t)\exp(-\alpha z). \quad (6)$$

where $R$is the surface reflectance, α is the absorption coefficient, $I(t)$ is the temporal laser intensity, and z is the depth measured from the laser-incident side of the T1107 layer. For a flat-top laser pulse, I(t) is expressed by equation (7).

$$I(t) = \begin{cases} \frac{F}{\tau_p}, 0 < t < \tau_p \\ 0, \quad t > \tau_p \end{cases}. \quad (7)$$

where $F$is the laser energy density and $\tau_p$is the pulse duration. Based on optical characterization at 308 nm, the 2.2-μm-thick T1107 layer absorbed approximately 90.2 % of the incident laser energy after accounting for surface reflection.

To accurately represent the depth-dependent absorption profile, the T1107 layer was divided into 10 sublayers along the thickness direction. The absorbed energy fraction assigned to each sublayer was calculated by equation (8).

$$A_i = (1-R)[\exp(-\alpha z_{i-1}) - \exp(-\alpha z_i)]\,. \quad (8)$$

where A_i denotes the absorbed energy fraction in the i-th sub-layer, and $z_{i-1}$and z_i are the upper and lower boundaries of that sublayer, respectively. This discretized approach enabled the model to capture the strong localization of laser heating near the irradiated interface. The initial temperature of all layers was set to room temperature. Perfect thermal contact was assumed at all interfaces, and the continuity of temperature and heat flux was imposed across the interfaces. Because the laser pulse duration was extremely short, the convective and radiative heat losses from the outer surfaces

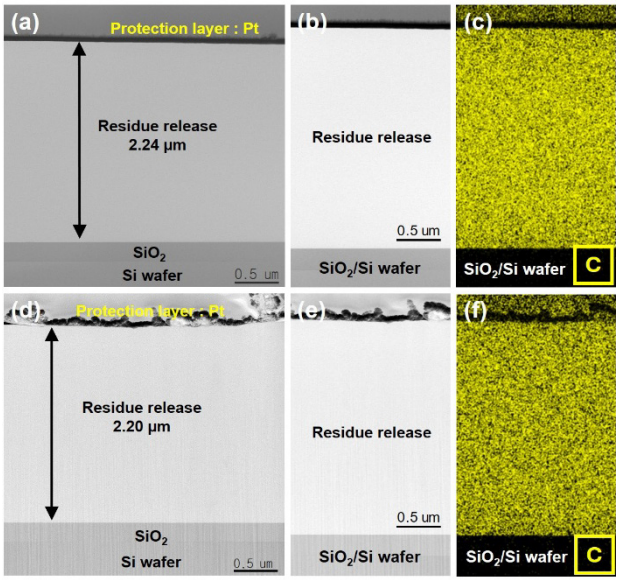

Fig. 8 Analysis of the residual release layer in a laser-debonded specimen from the inverse-structure TBW. Experimental parameters: 260 mJ/cm^2 and single shot: (a) TEM image of the residual release layer on the glass wafer, (b) STEM image for EDS analysis, (c) and EDS mapping of C from (b). Experimental parameters: 220 mJ/cm^2 and 5 shots: (d) TEM image of the residual release layer on the glass wafer, (e) STEM image for EDS analysis, and (f) EDS mapping of C from (e).

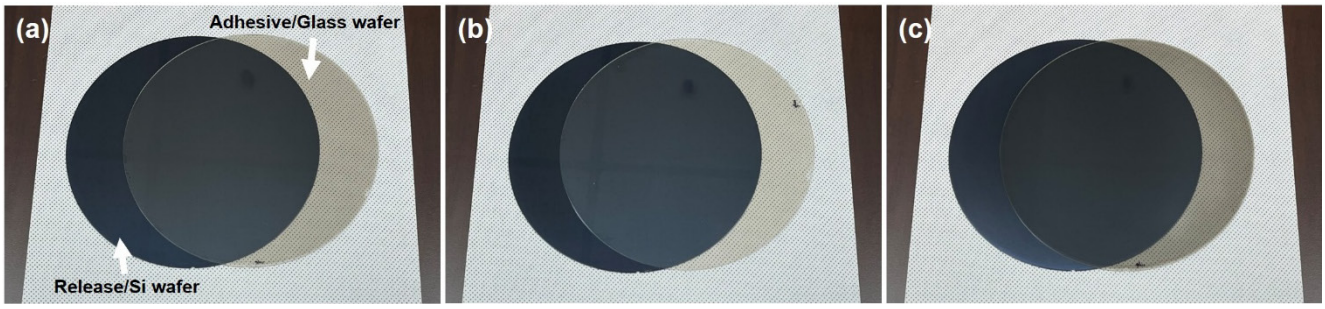

Fig. 9 Digital photos of debonded specimens from inverse-structure TBWs: (a) 260 mJ/cm^2 and single shot (0 % beam overlap), (b) 220 mJ/cm^2 and single shot (0 % beam overlap), and (c) 220 mJ/cm^2 and 5 shots (80 % beam overlap).

were neglected during irradiation. In our study, the simulation is intended to provide a thermal interpretation of the laser debonding behavior, rather than a complete multiphysics description of the process including photochemical effects, thermoelastic stress waves, and hot stamping effects. The model predicts the transient temperature rise, depth-dependent thermal distribution, and regions where the local peak temperature exceeds the thermal decomposition temperature of T1107, thereby estimating the decomposed region and residual thickness. Therefore, this thermal-threshold approach provides a reasonable basis for interpreting the debonding behavior and process window.

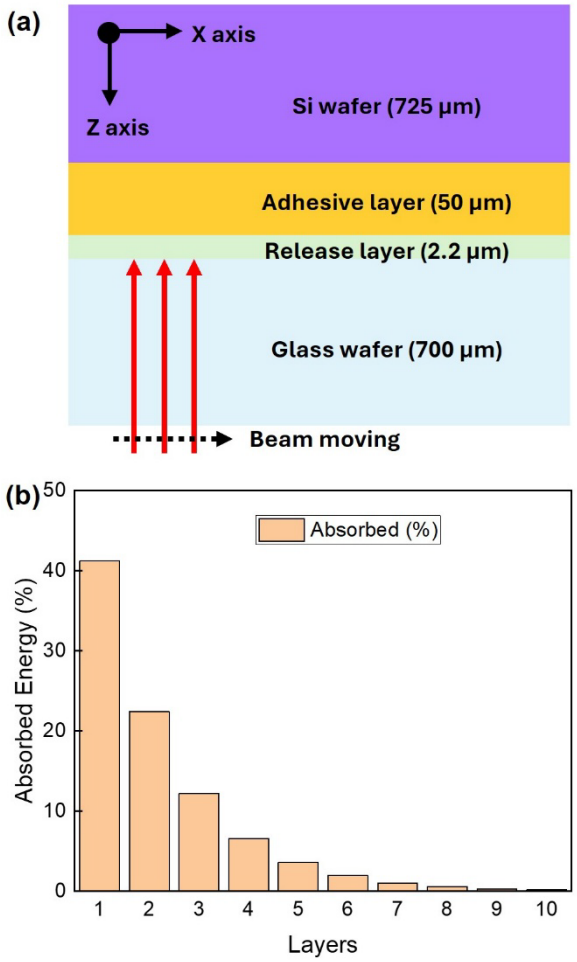

Fig. 10. (a) Schematic representation of the standard structure TBW, (b) depth-dependent energy absorption distribution in the release layer at a wavelength of 308 nm based on the Beer–Lambert law.

To correlate the simulation with the experimental debonding behavior, the decomposition region in the release layer was estimated using the thermal decomposition temperature (T_d) T1107 (T_d = 465 °C). The boundary between the decomposed and intact regions was defined as the depth at which the local peak temperature became equal to T_d. The residual thickness was defined as the remaining thickness of the release layer that did not exceed T_d. This definition enabled comparison between the simulated thermal response with the experimentally observed residual thickness after laser debonding.

Figure 10 shows a schematic of the simulation model and a graph of the calculated absorbed energy for each layer of T1107. Given the extremely high extinction coefficient of T1107 at 308 nm, analytical calculations based on the Beer–Lambert law demonstrated an exponential decay in the absorbed energy. Specifically, the discretized absorption profile revealed that the first 0.2-μm-thick sublayer, directly adjacent to the glass interface, absorbed the largest fraction of the energy, reaching approximately 41 %. The absorbed energy decreased sharply in the subsequent sublayers, with the second and third layers absorbing approximately 22 and 12 %, respectively. Consequently, over 75 % of the effective laser energy was highly concentrated within the first 0.6 μm of the T1107.

Figure 11 shows the cross-sectional temperature distribution of the standard structure at a laser energy density of 220 mJ/cm^2. The high-temperature region was highly localized near the interface between T1107 and the glass wafer. To quantitatively evaluate debonding efficiency, one-dimensional temperature profiles along the depth direction (cross-sectional line A-A') were extracted at various laser energy densities and are plotted in **Fig. 11(b).** The results indicate that at 200 mJ/cm^2, the peak temperature remained below the thermal decomposition temperature (T_d = 465 °C) of T1107. This insufficient heating explains the experimental debonding failure at 200 mJ/cm^2 under a single shot (as shown in Fig. 4(a)). When the energy density reached 220 mJ/cm^2, the peak temperature increased to 481 °C, exceeding the T_d threshold and initiating photothermal decomposition of the release layer. In the temperature profile, the exact depth at which the temperature dropped below T_d clearly delineate the decomposed region from the intact material. The intact unmelted portion of the release layer remaining on the glass wafer was defined as the residual thickness. The simulation further demonstrated that a higher laser energy density promoted deeper heat penetration into T1107 before the temperature decreased below T_d. Consequently, as the energy

density increased from 220 to 300 mJ/cm^2, the predicted residual thickness gradually decreased from 90 to 40 nm. This trend is remarkably consistent with the HRTEM observations, which demonstrated an actual residue thickness of approximately 49.11 nm at a fluence of 240 mJ/cm^2 (Fig. 5(b)).

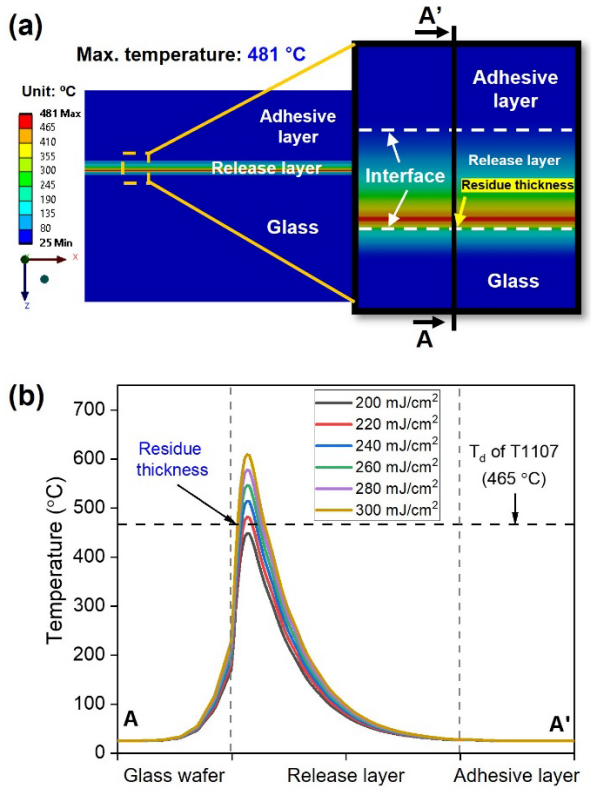

Fig. 11 Thermal simulation results for the standard structure TBW: (a) cross-sectional temperature distribution at laser energy density of 220 mJ/cm^2 and (b) temperature profile along A–A′ at different laser energy densities.

Figure 12 shows the simulation results for the inverse structure TBW. The thermal distribution and maximum temperature were comparable to those of the standard structure. This result indicates that the highly transparent adhesive layer (C1301) did not significantly interfere with optical absorption or heat transfer during the nanosecond laser pulse. This theoretical finding is in good agreement with the experimental results shown in Fig. 4, where the process windows (energy density vs. shot number) for both the standard and inverse structures were nearly identical. Consequently, both the simulation and experimental results clearly demonstrated that the inverse structure is a highly viable approach for advanced packaging, offering equivalent debonding efficiency with the additional advantage of simplified post-debonding cleaning on the device wafer.

4. Conclusion

In this study, laser debonding experiments were systematically performed using a 308 nm excimer laser and temporary bonding materials supplied by BrewerBOND. Temporary bonding specimens were prepared using a release layer (T1107) and an adhesive layer (C1301) in both standard and inverse structures to identify the appropriate energy densities and shot numbers. When the energy density exceeded

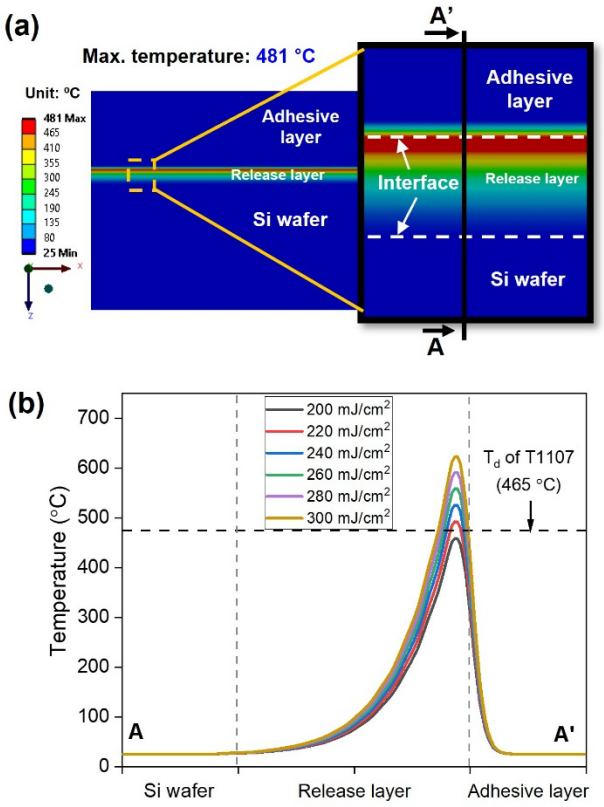

Fig. 12 Thermal simulation results for the inverse structure TBW: (a) cross-sectional temperature distribution at laser energy density of 220 mJ/cm^2 and (b) temperature profile along A–A′ at different laser energy densities.

220 mJ/cm^2, successful debonding was achieved with a single laser shot (0 % overlap) and no significant differences in process windows were observed between the standard and inverse structures. This behavior is attributed to the fact that debonding occurred exclusively via thermal decomposition at the surface of the release layer, which selectively absorbs 308 nm laser radiation. However, a clear difference was observed in the post-debonding residue, depending on the bonding configuration. The standard structure requires a two-step chemical cleaning process to remove both the release (~2.2 μm) and adhesive layers (~45 μm). Conversely, the inverse structure simplifies the cleaning process, as it only requires the removal of the release layer. Therefore, when TBM materials, including adhesive materials that are transparent at the laser wavelength, are employed, the inverse structure appeared to be more favorable from a post-debonding cleaning perspective. Furthermore, no thermal damage or degradation of the released material induced by laser irradiation was observed in the inverse structure. Based on these results, reliable laser debonding without thermal damage is expected to be achievable in practical demonstration samples that incorporate microbumps.

Acknowledgments

This work was supported by the Korea Evaluation Institute of Industrial Technology (KEIT) (Project No. RS-2024-00418649).

References

[1] M. D. Kumar, V. N. Sekhar, B.S.S. C. Rao, S. C. Chong, and V. S. Rao: Proc. 74th Electronic Components and Technology Conference (ECTC), (2024) 614.
[2] C. Wang, M. Zhang, X. Ming, S. Ma, and D. Yu: Microsyst. Technol., 27, (2021) 4121.
[3] K. Hwang, K.-S. Kim, B. Gorrell, K.-W. Kim, Y.-S. Yang, and W. Zou: Proc. 71st Electronic Components and Technology Conference (ECTC), (2021) 754.
[4] J. Liu, J. Li, T. Wang, D. Huang, Z. Li, A. Zhong, W. Liu, Y. Sui, Q. Liu, F. Niu, G. Zhang, and R. Sun: Polymer, 244, (2022) 124660.
[5] Z. Mo, F. Wang, J. Li, Q. Liu, G. Zhang, W. Li, C. Yang, and R. Sun: Electronics, 12, (2023) 1666.
[6] S. Wang, Y. Yu, S. Li, Y. Feng, J. Li, C. Yang, and W. Li: Appl. Opt., 62, (2023) 6140.
[7] T. Sounart, T. Talukdar, H. Braunisch, A. Aleksov, K. Jun, A. Elsherbini, P. Nordeen, B. Rawlings, V. Strong, S. Liff, and J. Swan: Proc. 74th Electronic Components and Technology Conference (ECTC), (2024) 363.
[8] F. Wang, Q. Liu, J. Li, M. Huang, W. Dai, X. Wang, G. Zhang, and R. Sun: Opt. Laser Technol., 169, (2024) 110169.
[9] J. Zhang, Y. Hu, F. Wang, Q. Liu, F. Niu, J. Li, M. Huang, G. Zhang, and R. Sun: Int. J. Extrem. Manuf., 7, (2025) 015005.
[10] W. Dai, J. Zhang, F. Wang, Q. Liu, M. Huang, T. Wang, G. Zhang, B. Zhou, and R. Sun: Appl. Surf. Sci., 687, (2025) 162219.
[11] C. Ma, F. Wang, H. Liu, Q. Liu, W. Dai, M. Huang, G. Zhang, and R. Sun: Appl. Surf. Sci., 721, (2026) 165350.
[12] W. Zhao, Y. Zeng, F. Wang, Q. Liu, W. Dai, M. Huang, G. Zhang, and R. Sun: Opt. Laser Technol., 199, (2026) 114956.
[13] F. Wang, Q. Liu, J. Xia, M. Huang, X. Wang, W. Dai, G. Zhang, D. Yu, J. Li, and R. Sun: Adv. Mater. Technol., 8, (2023) 2201186.
[14] Y. Kim, Y. Noh, S. Park, B.-K. Kim, and H. J. Kim: Int. J. Heat Mass Transf., 147, (2020) 118896.
[15] J. Bian, F. Chen, H. Ling, N. Sun, J. Hu, and Y. Huang: Int. J. Heat Mass Transf., 188, (2022) 122609.
[16] J. Hong, P. Cheng, J. Guo, W. Chen, Y. Li, J. Liu, Q. Zhu, and J. Chen: Surf. Interfaces, 36, (2023) 102561.
[17] I. Choi, X.-B. Le, S.-H. Choa, J. Suh, S. Mo, and S. Lee: J. Microelectron. Packag. Soc., 32, (2025) 55.
[18] B. Lukyanchuk, N. Bityurin, M. Himmelbauer, and N. Arnold: Nucl. Instrum. Methods Phys. Res. B, 122, (1997) 347.
[19] N. Bityurin and A. Malyshev: J. Appl. Phys. 92, (2002) 605.

(Received: April 21, 2026, Accepted: July 26, 2026)